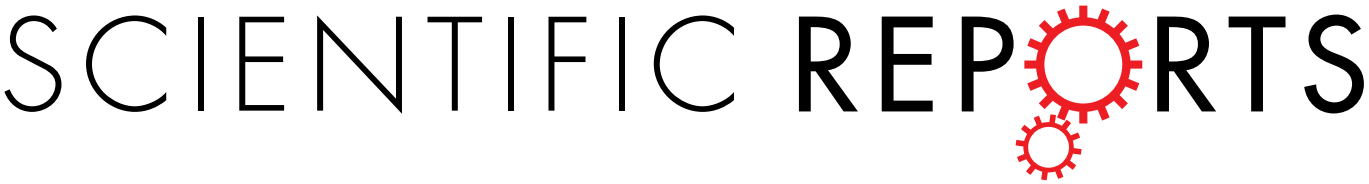

OPEN

# Data-driven Modeling of Hemodynamics and its Role on Thrombus Size and Shape in Aortic Dissections

Received: 8 September 2017
Accepted: 22 January 2018
Published online: 06 February 2018

Alireza Yazdani[1], He Li[1], Matthew R. Bersi[2], Paolo Di Achille[2], Joseph Insley[3], Jay D. Humphrey[2], & George Em Karniadakis[1]

**Aortic dissection is a pathology that manifests due to microstructural defects in the aortic wall. Blood enters the damaged wall through an intimal tear, thereby creating a so-called false lumen and exposing the blood to thrombogenic intramural constituents such as collagen. The natural history of this acute vascular injury thus depends, in part, on thrombus formation, maturation, and possible healing within the false lumen. A key question is: Why do some false lumens thrombose completely while others thrombose partially or little at all? An ability to predict the location and extent of thrombus in subjects with dissection could contribute significantly to clinical decision-making, including interventional design. We develop, for the first time, a data-driven particle-continuum model for thrombus formation in a murine model of aortic dissection. In the proposed model, we simulate a final-value problem in lieu of the original initial-value problem with significantly fewer particles that may grow in size upon activation, thus representing the local concentration of blood-borne species. Numerical results confirm that geometry and local hemodynamics play significant roles in the acute progression of thrombus. Despite geometrical differences between murine and human dissections, mouse models can provide considerable insight and have gained popularity owing to their reproducibility. Our results for three classes of geometrically different false lumens show that thrombus forms and extends to a greater extent in regions with lower bulk shear rates. Dense thrombi are less likely to form in high-shear zones and in the presence of strong vortices. The present data-driven study suggests that the proposed model is robust and can be employed to assess thrombus formation in human aortic dissections.**

Dissection of the thoracic aorta is a life threatening event; it is responsible for significant morbidity and mortality in individuals ranging in age from children to young and old adults alike. Dissection can result from blunt trauma, but it often associates with aneurysmal dilatation and heritable connective tissue disorders, including Marfan syndrome, familial thoracic aortic aneurysm, Loeys-Dietz syndrome, Ehlers-Danlos syndrome, and so forth[1]. These dissections often propagate within the medial layer and connect with the true lumen to form a false lumen within the aortic wall, which in turn can remain patent, become partially thrombosed, or be completely filled with thrombus.

Thrombus formation is the normal physiologic response to prevent significant blood loss upon vascular injury, but its role in different disease conditions can be detrimental. Clinical findings increasingly suggest, for example, that patients with a partially thrombosed dissection are at a higher risk of rupture[2]. Conversely, completely thrombosed dissections have a better prognosis[3]. Indeed, it has been suggested that "complete thrombosis of the residual false lumen might be a sign of aortic wall healing and remodeling"[4].

There has been a growing interest in the use of mouse models in vascular biology due to their availability and broad phenotypes, especially compared with other animal models. Most notably, chronic infusion of angiotensin

[1]Division of Applied Mathematics, Brown University, Providence, RI, 02912, USA. [2]Department of Biomedical Engineering, Yale University, New Haven, CT, 06520, USA. [3]Argonne National Laboratory, Argonne, IL 60439; Northern Illinois University, DeKalb, IL, 60115, USA. Alireza Yazdani and He Li contributed equally to this work. Correspondence and requests for materials should be addressed to A.Y. (email: alireza_yazdani@brown.edu) or G.E.K. (email: george_karniadakis@brown.edu)

II (AngII) in male apolipoprotein-E null ($ApoE^{-/-}$) mice yields a reproducible model of dissecting aortic aneurysm, which often includes a false lumen with intramural thrombosis[5]. Although medical imaging now enables us to quantify the subject-specific geometry of the false lumen and to construct associated computational fluid dynamics models in both human and murine dissections[6–9], no existing model can predict the development, growth, or arrest of an intramural thrombus. The present data-driven study is significant for it elucidates, for the first time, hemodynamic conditions under which an intramural thrombus forms in aortic dissections.

Quantifying continuum-level hemodynamics is fundamental for many reasons:[10,11] circulating blood is the source of, amongst other components, the platelets, fibrinogen, and plasminogen that enable the thrombus to develop and subsequently remodel; increased fluid shear stresses can activate platelets; increased residence times within regions of low flow can promote platelet aggregation; and high shear rates can limit thrombus expansion into the flow field. Including the effects of platelets is particularly important in any numerical model that targets thrombus formation. Whole blood is commonly considered an incompressible Newtonian (or non-Newtonian) fluid in large arteries; this leads to continuum fields for blood velocity and pressure. The concentration of blood borne biomolecules can be resolved similarly using advection-diffusion-reaction equations, which provide spatio-temporal information on the concentration of, for example, fibrinogen (the precursor to fibrin) and plasminogen (the precursor to plasmin). Individual or groups of platelets, in contrast, can be treated as Lagrangian particles. Building on our recent study[12], we develop a particle-continuum model based on a force coupling method (FCM) that provides a flexible platform for *two-way coupling* of platelets (treated as semi-rigid spherical particles) and the background continuum flow. As a result, thrombus size and shape is affected by the local hemodynamics, particularly fluid stresses. Further, it is possible to include porosity of the forming thrombus by adjusting the radius of influence of each particle on the fluid as discussed in "Methods".

While continuum-level hemodynamics plays a crucial role in thrombus formation as well as its final size and shape within a false lumen, the cellular and sub-cellular-scale hemostatic processes (*e.g.*, platelet adhesion, aggregation, and coagulation kinetics) must be taken into account in any multiscale model (see *e.g.*[13–15]). We propose here a data-driven multiscale numerical approach to address thrombus formation in dissecting geometries, whose length scales are significantly larger than microscopic scales encountered at the cellular levels. An additional challenge in modeling thrombosis is the long physiologic time-scales in the evolution of intramural thrombus, and its subsequent remodeling within the false lumen. Here, we take advantage of the apparent time-scale separation in this biological process that decomposes it into two main sub-processes, namely *acute thrombus formation* and the subsequent *growth and remodeling* of thrombus and the remnant wall.

## Results

Consider, first, the computed flow fields within each of three lesions (Fig. 1) with thrombus removed numerically. Results are represented as flow streamlines (colored by velocity magnitude) at peak systole, and without particles, to understand the pattern and strength of vortices that might contribute to thrombus deposition. It is noteworthy that the Reynolds number (*Re*, defined by the diameter and mean blood flow velocity at the proximal aorta) is similar for these three lesions, with $Re \approx 30$. The patterns of the vortical zones, however, differ markedly by lesion and are affected mainly by the size of the opening into the false lumen. The small orifice (Fig. 1c) leads to the smallest vortex, whereas the orifice of the medium false lumen (Fig. 1b) allows the circulation zone to grow in size. More notably, the large orifice size in the large dissection (Fig. 1a) causes the flow to break into two significantly larger vortices inside the false lumen close to peak systole. Note, therefore, that Philips *et al*. analyzed $\lambda_2$ distributions to detect regions of vortical flows inside the same lesions[16]. They showed that negative $\lambda_2$ regions form initially close to the proximal end of the false lumen opening and persist inside the false lumen for large parts of the cardiac cycle, consistent with results shown in Fig. 1.

To quantify the effects local shear rate on the non-Newtonian rheology of blood, we first estimated the scalar shear rate for these three lesions. The results for $\dot{\gamma} = \sqrt{2\mathbf{D}:\mathbf{D}}$ are shown in Fig. 1 for the three lesions, where $\mathbf{D} = (\nabla\mathbf{u} + \nabla\mathbf{u}^{\mathrm{T}})/2$ is the symmetric part of the spatial velocity gradient. In all lesions, we observe regions of weak flow, with local shear rates $<10\,s^{-1}$ only at the two ends of the false lumen. Using an empirical correlation for blood non-Newtonian rheology such as the Carreau-Yasuda model[17] we estimate a three-fold increase in shear viscosity with respect to the physiologic value $\mu = 0.004\,Pa.s$. Our simulations have shown that thrombus formation initiates first in the ends of the false lumen, which is followed by flow stagnation; non-Newtonian effects are negligible in all other regions.

Figure 2 shows snapshots of particle distributions in the false lumen, where adhered particles in the thrombus are slightly larger than other particles. The streamlines also show a major vortex close to the orifice, which creates a hydrodynamically active region with significantly less particle adhesion and thrombus deposition. Continuum FCM volume fractions were calculated based on the adhered pseudo-particle positions using the FCM Gaussian kernel given in Eq. (10). As will be shown later (based on volume fractions $\phi_{fcm}$), our numerical simulations with FCM particles suggest that the size and shape of these vortices are significant determinants of final thrombus deposition inside the false lumen.

**Thrombus size and shape.** *Parameter estimation and sensitivity analysis.* Two main parameters that affect thrombus deposition within the false lumen are the strength of the adhesive forces $D_e$ and the effective particle radius $r_{eff}$. Whereas the value of $r_{eff}$ directly affects the cost of the simulations, since a lower effective radius implies a significantly higher number of particles $\left(N_p \sim r_{eff}^{-3}\right)$, it also improves the predicted final shape that is otherwise driven by $D_e$.

Noting that the clot volume fraction is a heterogenous spatial field ($\phi \equiv \phi(x, y, z)$), we quantified the variation of $\phi$ along the primary flow direction ($z$−axis) by integrating it on each planar cross section, namely $\phi_z = 1/A_{sec} \int\phi(x, y, z)\, dxdy$, where $A_{sec}$ is the area covered by thrombus in each cross section. First, consider the evolution of clot volume fraction within the false lumen in Fig. 3a for $D_e = 2 \times 10^{-3}$ and $r_{eff} = 20r_p$. The results show an initial

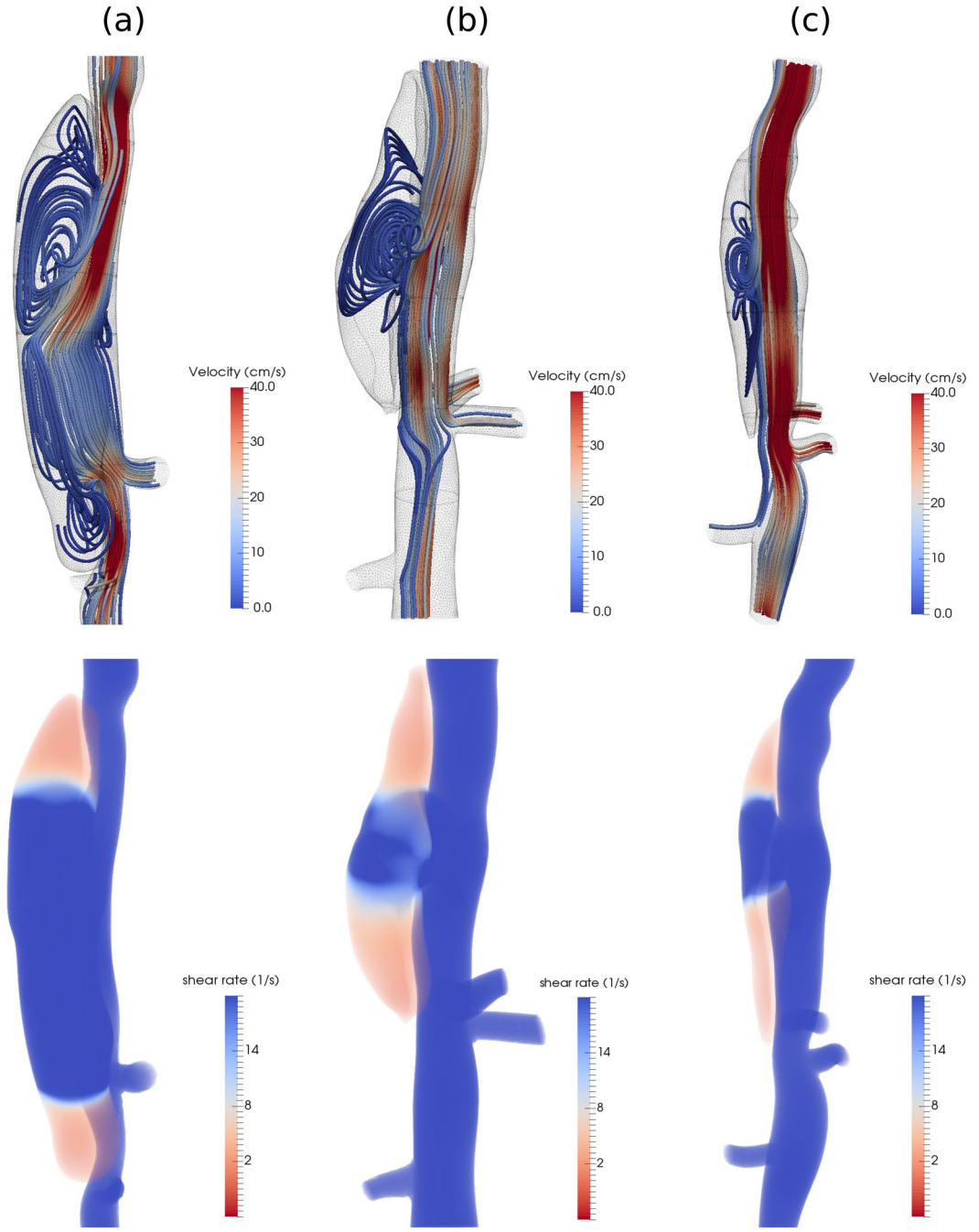


**Figure 1.** Top row: Snapshots of flow streamlines colored by velocity magnitude at peak systole for the three lesions (blood flow is from top to bottom in all cases). Bottom row: Volume rendering of time-averaged scalar shear rate $\dot{\gamma}$ over one cardiac cycle within the false lumen. The Reynolds number for each lesion is 24.4, 32.5, 24.3, for the (**a**) large, (**b**) medium, and (**c**) small false lumen, respectively.

sudden increase in $\phi_z$ followed by a gradual increase towards its quasi-static distribution at $t^* = 100$, which is equivalent to approximately 10 cardiac cycles. Further, $\phi_z$ is plotted for three different values of $r_{eff} = 20r_p$, $30r_p$, $40r_p$ in Fig. 3b for comparison. The distributions of $\phi_z$ show a qualitative agreement for different effective radii at the two ends of the lesion (*i.e.*, $z > 1$ and $z < -1$), whereas the results show significant deviations close to the orifice of the false lumen. An effective radius $r_{eff} = 40r_p$ overestimates the shape of the thrombus at the opening, whereas the average volume fraction for $r_{eff} = 30r_p$ and $r_{eff} = 20r_p$ does not clearly show which one of the effective radii predicts better the thrombus size and shape; hence, a detailed analysis of thrombus shape similar to Fig. 4 is required.

The effect of adhesive force coefficient $D_e$ is plotted in Fig. 4a–c for particles with radius $r_{eff} = 30r_p$, recalling that we seek agreement between the simulated (defined by the red boundaries in Fig. 4) and the experimental, as measured by optical coherence tomography (OCT) (defined by dark boundaries in Fig. 4), thrombus. Here, we

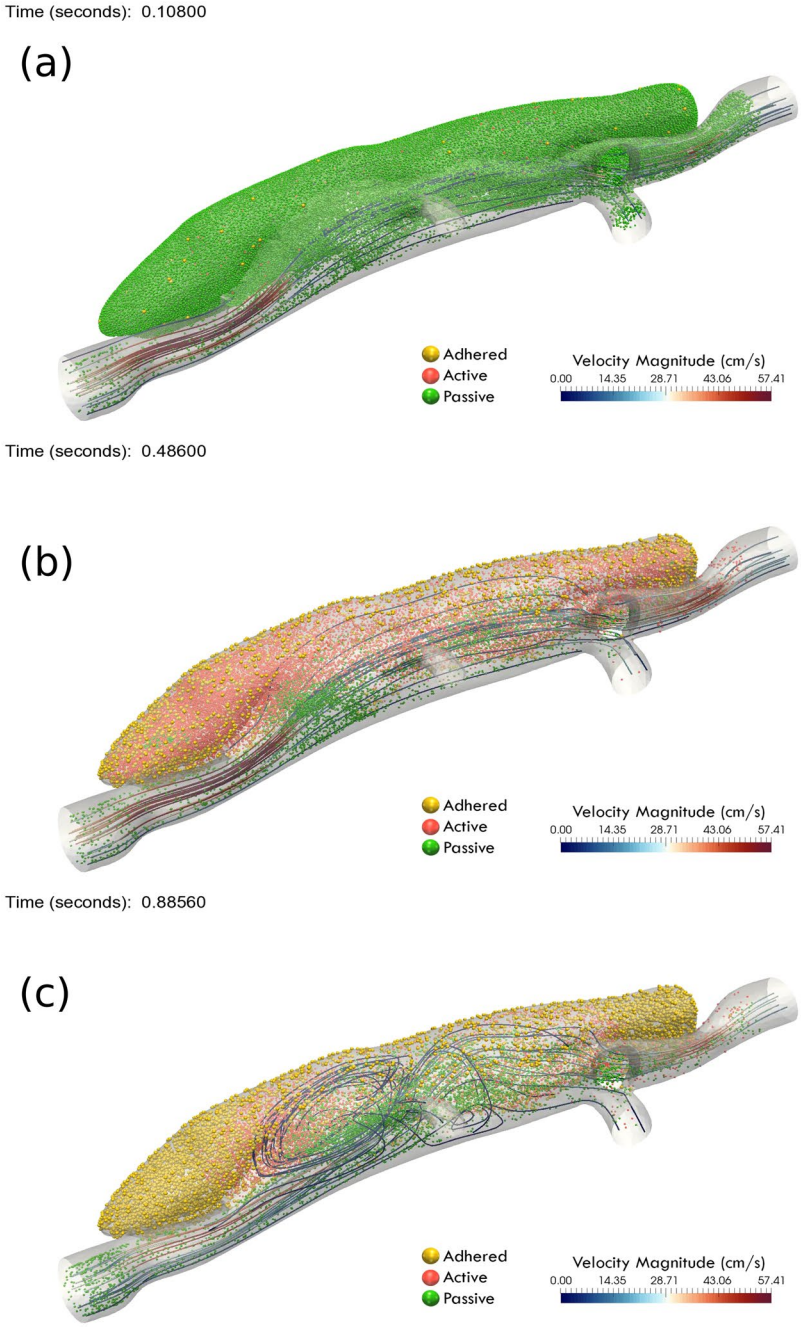


**Figure 2.** Snapshots of particle distributions in the large false lumen at three different times during the simulation: (**a**) initial particle distribution; (**b**) intermediate stage at end diastole; (**c**) final stage at peak systole, along with a small number of representative flow streamlines colored by velocity magnitude. Particle color codes are: passive particles (green); active or triggered particles (red); active and adhered particles (yellow). Not all particles are shown for clarity, and flow is from left to right.

focus on the lesion with the medium false lumen and vary $D_e$ in the range of $2 \times 10^{-4}$ to $5 \times 10^{-3}$ (nondimensional units), while keeping $r_{eff} = 30r_p$ (Fig. 4a–c). The best agreement was achieved for $D_e = 2 \times 10^{-3}$ (except for the overestimation close to section C). Reducing $D_e$ by an order of magnitude (shown in Fig. 4b relative to Fig. 4c) caused the FCM to perform poorly in regions where the flow field is highly active with strong vortices (sections C and D), though all simulations captured thrombus size and shape well at the two ends of the false lumen (sections A and F), due to the weak flow dynamics (cf. Fig. 1). A further increase in $D_e$ to $5.0 \times 10^{-3}$ overestimated the size and shape of the thrombus in the active vortical zone (sections C and D, Fig. 4c) where adhesive forces are relatively high. Our simulations for all three lesions suggest that an adhesive force coefficient $D_e = 2 \times 10^{-3}$ is appropriate for modeling the adhesion of pseudo-particles.

In addition to the choice of adhesive force, the effective radius of the activated particles plays an important role in determining the size and shape of the thrombus. As suggested by Fig. 3, the value of $r_{eff} = 30r_p$ overestimated the

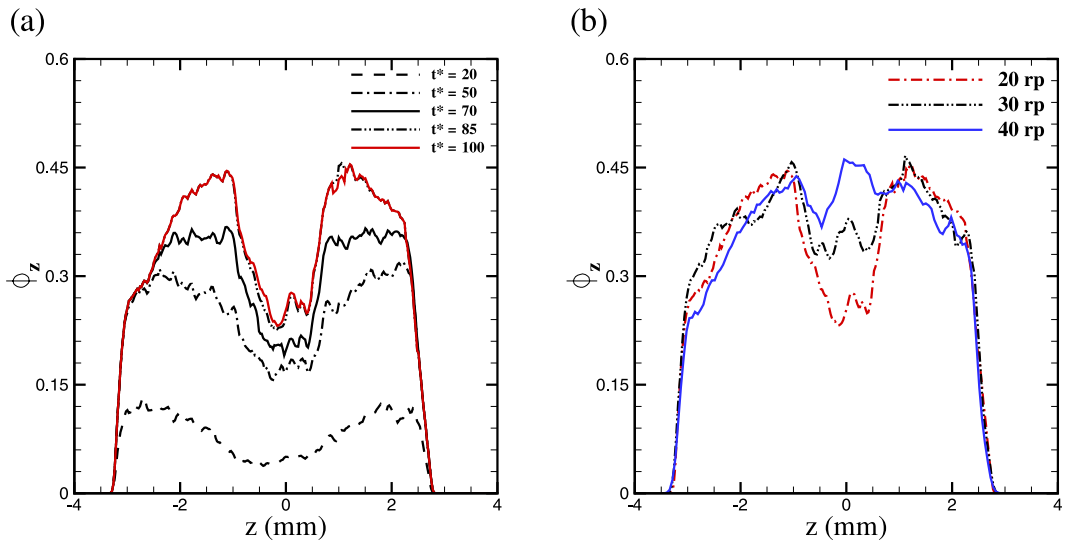


**Figure 3.** Average volume fraction of the clot $\phi_z$ computed in each cross section along the flow direction in the medium false lumen. (**a**) Temporal simulations suggest that clot volume fraction stabilizes after 10 cycles. (**b**) Simulations for different values of particle radius $r_{eff}$ suggest that smaller particle radius is more effective in capturing thrombus size and shape.

thrombus volume fraction and size, especially in regions of higher fluid shear stresses. Hence, we used $r_{eff} = 20r_p$ in our simulations for all three lesions, which led to better predictions of thrombus shapes.

It is known that enhanced diffusion of platelets occurs due to collisions with red blood cells. This phenomenon has been studied extensively experimentally and theoretically, for straight channels and idealized vessels. Enhanced diffusion of platelets in a complicated geometry such as the false lumen, however, is rather intricate. It is known that enhanced diffusion depends on the local blood hematocrit and shear rates. For the range of shear rates encountered in this study, the effective diffusion coefficient for platelet particles is $D_{eff} \approx 10^{-11}\, m^2/s$. We included a shear-enhanced diffusion for the particles inside the false lumen by adding a Gaussian random displacement $(2D_{eff}dt)^{1/2}$ to each particle's position after integrating Eq. (5). The final shape of the thrombus remained almost unaffected by this additional term (data not shown), thus we did not include the random term in subsequent simulations. The insertion of particles at the proximal inlet, however, was informed by a master profile for platelet distribution taking into account their margination in the aorta[18].

*Acute evolution of thrombus size and shape.* Next, we consider the evolution of thrombus deposition in the medium false lumen in Fig. 5b, noting that thrombus formation is accelerated in our simulations within approximately 10 cycles due to increased size of an activated particle's effective radius. By monitoring different cross-sections along the false lumen, we observe faster thrombus growth and increased volume fractions closer to the ends, where $\phi_{fcm}$ can reach as high as 90% (results not shown). Closer to the orifice of the false lumen (sections B and C), however, simulations predict a partial thrombosis with a lower volume fraction, indicating a less dense thrombus close to the remnant wall.

We performed an analysis similar to Fig. 3 to identify when a quasi-stable thrombus shape had been reached in our simulations. Once the size and shape stabilize, we extracted the boundaries of the thrombus and compared them with thrombus geometries segmented from OCT images in[16] (see Fig. 5c for the medium false lumen). We achieved good agreements in less hydrodynamically active zones (sections A and D). In more active regions, the agreement was acceptable given the uncertainty in both the simulation parameters and experimental measurements (*e.g.*, OCT images have a spatial resolution ~7 $\mu m$). Most notably, the boundary of the false lumen in section C, which forms a ring (shown by an arrow in Fig. 5c), was captured in our simulation despite a slight offset in the location of the simulated false lumen relative to the experiment.

To further analyze the robustness of our model with respect to changes in the hemodynamic conditions, we performed further sensitivity analysis by varying the flow rate in the medium false lumen. We considered two scenarios in which we increased *Re* by a factor of two and decreased it by a factor of two. The final shapes of thrombus are plotted in Fig. 5 along with the simulation at the original *Re*. We observe that in regions with weaker flow (sections A and D) the thrombus shapes agree with the experiment very well for all three scenarios. The difference becomes more evident in sections B and C close to the orifice. Higher *Re* leads to underprediction in the size of thrombus close to section C, which is attributed to higher shear forces in those regions preventing a stable aggregation. At the lower *Re* we observe an underprediction in sections B and C following a reduciton in the flux of platelets from upstream due to lower flow rates.

Our simulations suggested a strong correlation between hemodynamic forces and final thrombus size and shape. To further examine this finding, we performed FCM simulations for two additional simulated lesions with different orifice sizes that created different hemodynamic environments (cf. Fig. 1). We present the evolution of

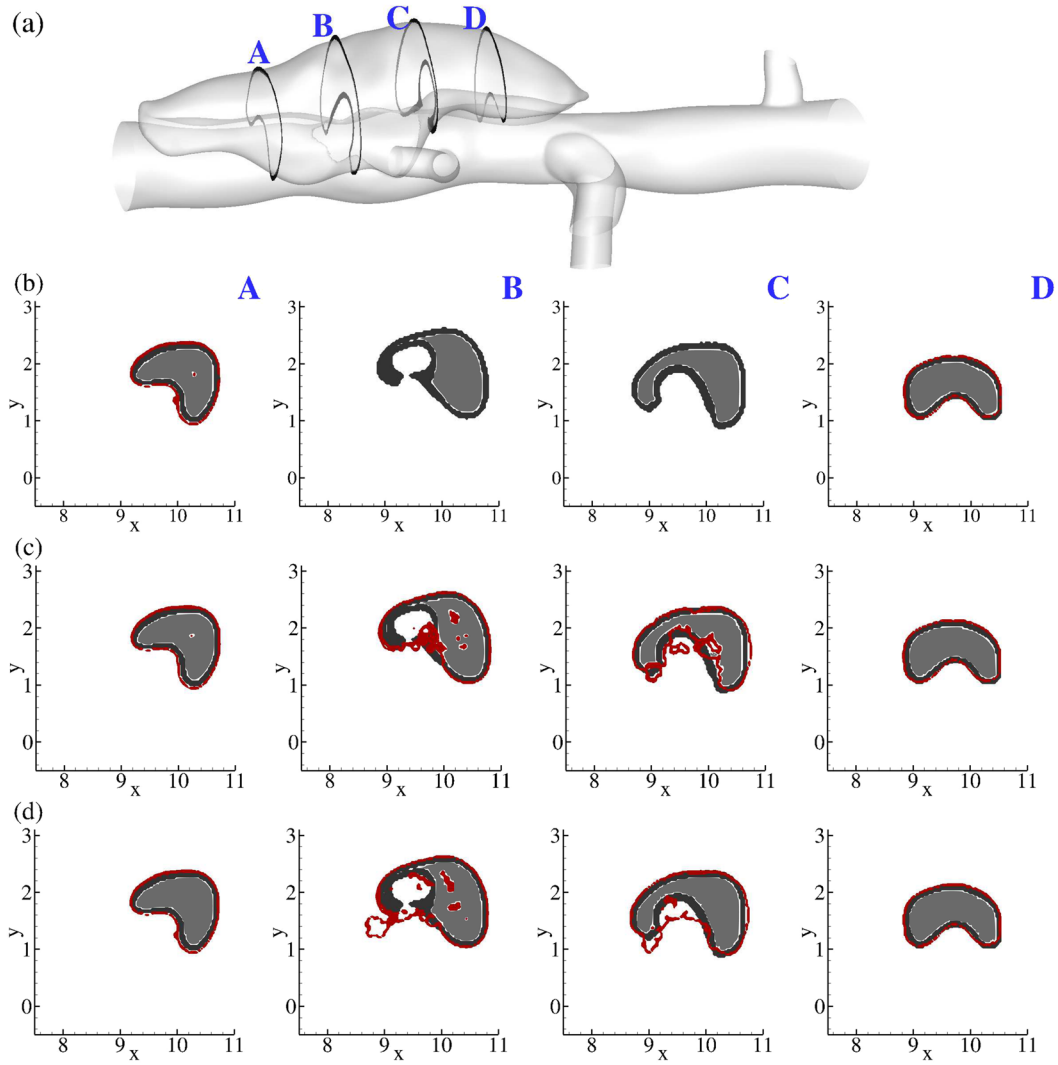


**Figure 4.** Effect of the adhesive force parameter $D_e$ on the size and shape of the clot (shown as an enclosed contour) for the medium false lumen for a fixed value of $r_{eff} = 30r_p$, where: (**b**) $D_e = 2 \times 10^{-4}$; (**c**) $D_e = 2 \times 10^{-3}$; (**d**) $D_e = 5 \times 10^{-3}$. Comparison at 4 different cross-sections along the flow direction (left to right, or A–D), where gray area show the segmented thrombus shape from OCT results and red contours are the simulation results.

thrombus formation for the small false lumen in Fig. 6b, for which the vortical structure close to the orifice is smaller than that for the medium false lumen as shown in Fig. 1c.

Note a fast growth of thrombus closer to the ends of the false lumen (*i.e.*, sections A and D), with the size of the patent lumen reduced significantly and limited to the vicinity of the orifice (section C). Taking into account the pattern of vortices in that region (Fig. 1c) and the direction of flow (along the $z$ axis), the effects of hemodynamics on the final size and shape are prominent. Further comparison of the final size and shape between simulation and experiment shows a good agreement in most regions of the false lumen, albeit with a slight underestimation in the size of thrombus at cross-section D. Close to the orifice, however, thrombus formed adjacent to the false lumen wall (section C), as predicted by the simulation.

Next we performed FCM simulations for the largest false lumen, which also had the largest orifice among the three lesions. The wider opening into the false lumen creates a significantly larger vortex than in the other two lesions, which breaks into two strong vortices close to peak systole (cf. Fig. 3b and supplementary video). These vortices, and the resulting shear forces, prevent platelets from aggregation and forming a firm and stable thrombus inside the false lumen along most of the width of the opening. This can be clearly observed from the evolving thrombus shape in Fig. 7b along sections B to D. The two ends of the false lumen form more stable thrombi, however, similar to other lesions due to weaker hydrodynamic forces present in those regions.

Comparison with experimental thrombus shape in Fig. 7c shows an underprediction of thrombus size at sections A and C. Section C lies at the center of the false lumen, where the two counter rotating vortices meet during peak systole and, thus, form a stagnant region. This could potentially result in a higher accumulation of platelets and their residence time in that small region depending on the initial distribution of platelets and other

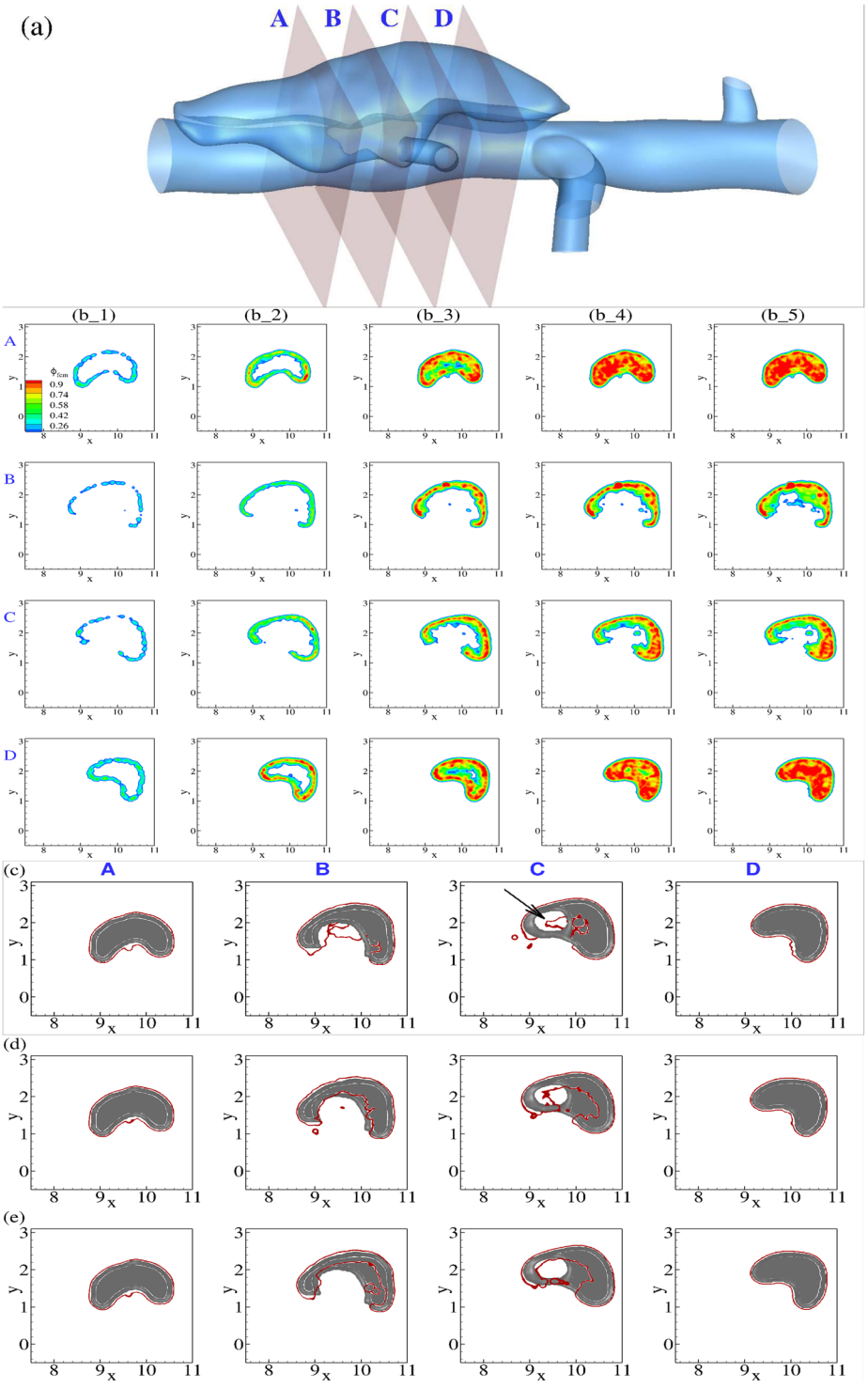


**Figure 5.** (**a**) Guide for planar cross-sections in the medium false lumen taken along the flow direction (flow from A to D). (**b**) Time evolution of continuum FCM volume fraction $\phi_{fcm}$ field for 4 cross-sections labeled as above. First column is plotted after the first 2 cardiac cycles, with time incremented 2 cardiac cycles for every subsequent column. (**c**–**e**) Cross-comparison of simulated thrombus boundaries extracted from panel (b_5) (red) with experimental thrombus shapes (gray) extracted from OCT images for flow dynamics at: (**c**) the original $Re = 32.5$; (**d**) twice higher $Re = 65$; (**e**) twice lower $Re = 16.3$. We note a shift in the predicted false lumen shown by an arrow at section C for the original *Re*, and underpredictions for other *Re* at this section.

coagulants in a dissecting aneurysm, which is not known precisely *a priori*. Further, we believe that the smaller size of thrombus close to section A (shown by the arrow in Fig. 7c) is due to significantly higher shear forces in that region compared to other lesions.

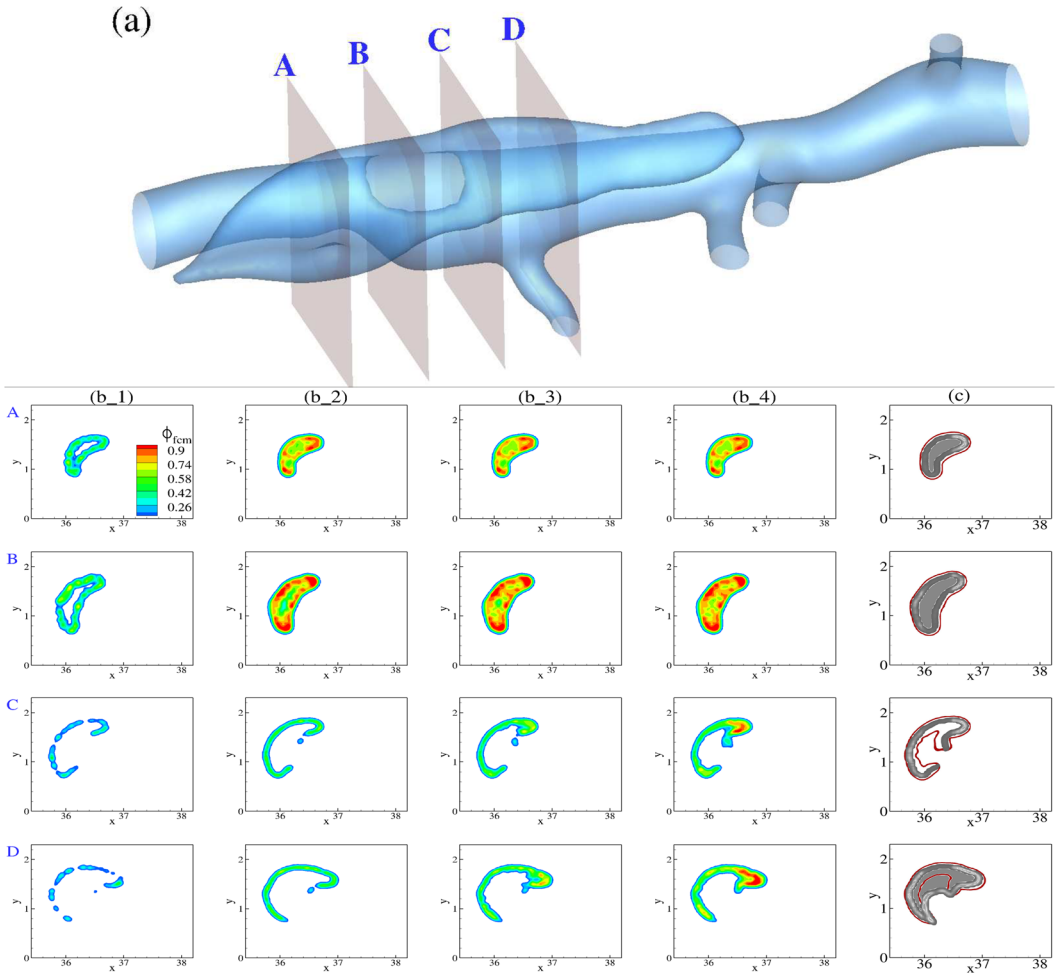


**Figure 6.** (**a**) Guide for planar cross-sections in the small false lumen taken along the flow direction (flow from A to D). (**b**) Time evolution of continuum FCM volume fraction $\phi_{fcm}$ field for 4 cross-sections labeled as above. First column is plotted after the first 2 cardiac cycles, with time incremented 2 cardiac cycles for every subsequent column. (**c**) Cross-comparison of simulated thrombus boundaries extracted from panel (b_4) (red) with experimental thrombus shapes (gray) extracted from OCT images.

The results show clear distinctions in the magnitude and location of high shear rates within the false lumen between large and medium lesions: higher shear rates ($\approx 500\, s^{-1}$) are present at peak systole inside the large false lumen, covering a wider region, whereas shear rates are close to $100\, s^{-1}$ in the medium false lumen (see Fig. 8a and c). One common pattern between these lesions is relatively weak shear rates near the ends of the false lumen, which are presumably sites where thrombus starts depositing. As thrombus progresses toward the center of the false lumen, it is subject to increasingly higher shear rates, which eventually prevent further thrombus formation. Hemodynamic simulations for the experimentally observed false lumens show distinct flow regimes and shear rates in these two lesions (see Fig. 8b and d). The shear rates remain relatively low, close to $100\, s^{-1}$, inside the final shape of the medium false lumen. In contrast, shear rates increase further inside the large false lumen, especially in the vicinity of the thrombus surface, thus preventing further thrombus formation and suggesting why the large false lumen remains nearly patent.

**Transport of fibrinogen and platelets in the false lumen.** Knowledge of local concentrations of fibrinogen (Fbg) and platelets inside the false lumen is essential to estimating the composition of thrombus. We performed pilot studies for the transport of Fbg and platelets inside the false lumen by solving the advection/diffusion Eq. (9). We set the normalized concentration of both species equal to 1 everywhere and performed simulations with zero flux boundary conditions for long periods (~10 cardiac cycles) to reach stable distributions inside the false lumen. Results for the medium and large false lumens are shown in Fig. 9.

Distributions show a similar pattern for Fbg and platelets for both medium and large false lumens in which the concentrations remain less affected by the flow close to the ends of the false lumen, where bulk shear rates are lower. At the center of the false lumen close to its opening, however, where shear rates are higher, we observe large regions depleted of Fbg and platelets. Interestingly, the depleted regions co-localized with regions of high bulk shear rates (see Fig. 8) and, thus, could be used as a guide for the extent of acute thrombus growth and the size of the final false lumen.

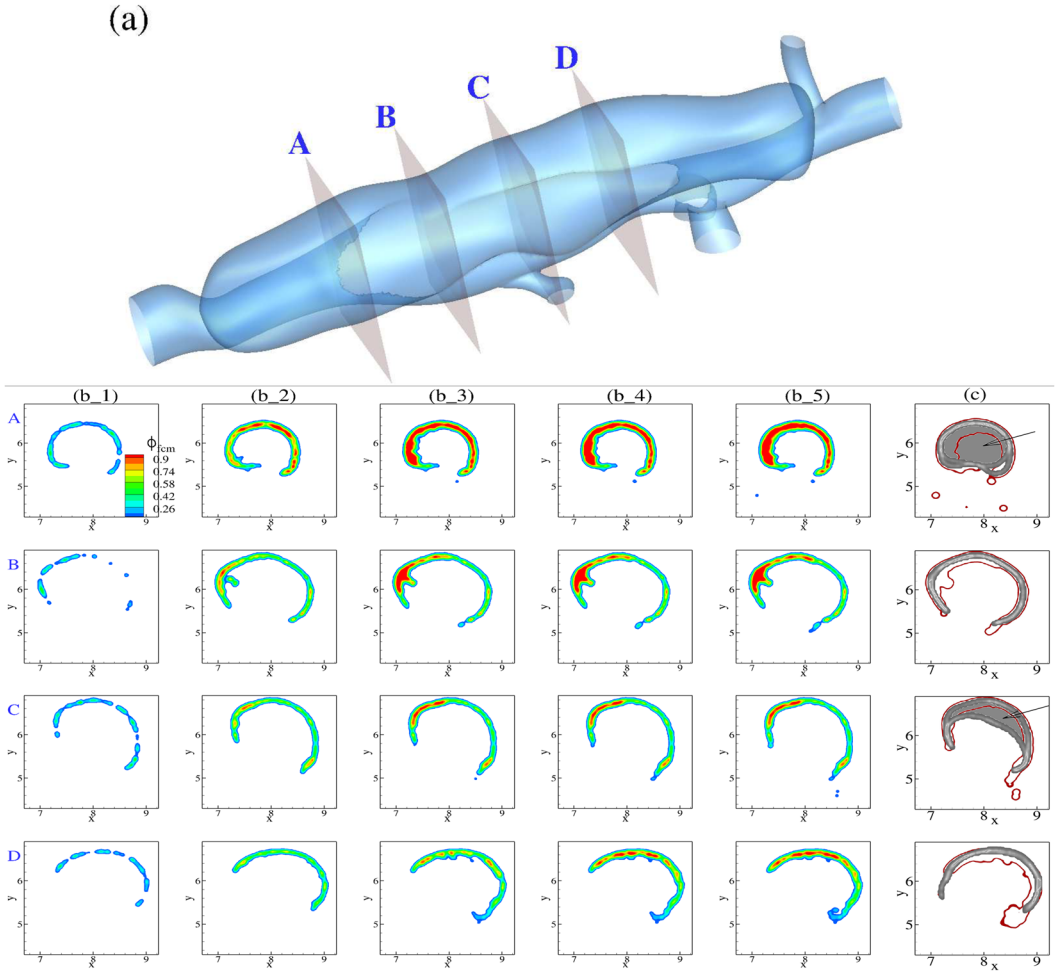


**Figure 7.** (**a**) Guide for planar cross-sections in the large false lumen taken along the flow direction (flow from A to D). (**b**) Time evolution of continuum FCM volume fraction $\phi_{fcm}$ field for 4 cross-sections labeled as above. First column is plotted after the first 2 cardiac cycles, with time incremented 2 cardiac cycles for every subsequent column. (**c**) Cross-comparison of simulated thrombus boundaries extracted from panel (b_5) (red) with experimental thrombus shapes (gray) extracted from OCT images. We note an underprediction by the simulation at sections A and C shown by the arrows.

## Discussion

Our subject-specific numerical results, based on three geometrically different lesions, suggest that the initial size and the shape of the false lumen and the size of its orifice are highly crucial in dictating the progression of thrombus formation inside the dissection. A salient feature of all three lesions is enhanced accumulation of thrombus at the ends of the false lumen, which associates with significantly lower local shear rates ($\ll 50\ s^{-1}$). Closer to the opening of the false lumen, however, stronger vortices and higher shear rates prevent further thrombus growth. These results suggest a threshold shear rate value below which thrombus is more likely to form, $\dot{\gamma}_{thr} \approx 100\ s^{-1}$. A more rigorous statistical analysis with more subjects would be needed to confirm this apparent threshold value, however.

It is acknowledged that murine aortic dissections differ from human dissections in terms of location, geometry, and extent of the false lumen. Human dissections often manifest as longitudinal false lumens that are typically very long, and may develop multiple proximal and distal tears. The Reynolds number of the hemodynamics are higher in the false lumen, which can cause secondary flows and different flow patterns. Numerical simulations of thrombus formation in patient-specific aortic dissections are relatively rare. In a recent study, Menichini *et al*[19]. proposed a thrombosis model for predicting the false lumen in patient-specific type B aortic dissections. The model is based on continuum fields of activated and resting platelets as well as most relevant coagulation enzymes. Although proposed for human dissections, the results are similar qualitatively to the present murine results in a sense that thrombus formation initiates in regions of low wall shear stress or equivalently low bulk shear rates.

The multiscale numerical method we propose is novel in that it is appropriate for both short-term and long-term processes (see Fig. 10), noting that the present study addressed only the first portion of the numerical approach, namely the modeling of initial thrombus deposition until a quasi-static shape has been reached. Clearly, the challenge in this problem is long-term simulation of particles actively coupled with flow. The complexities in

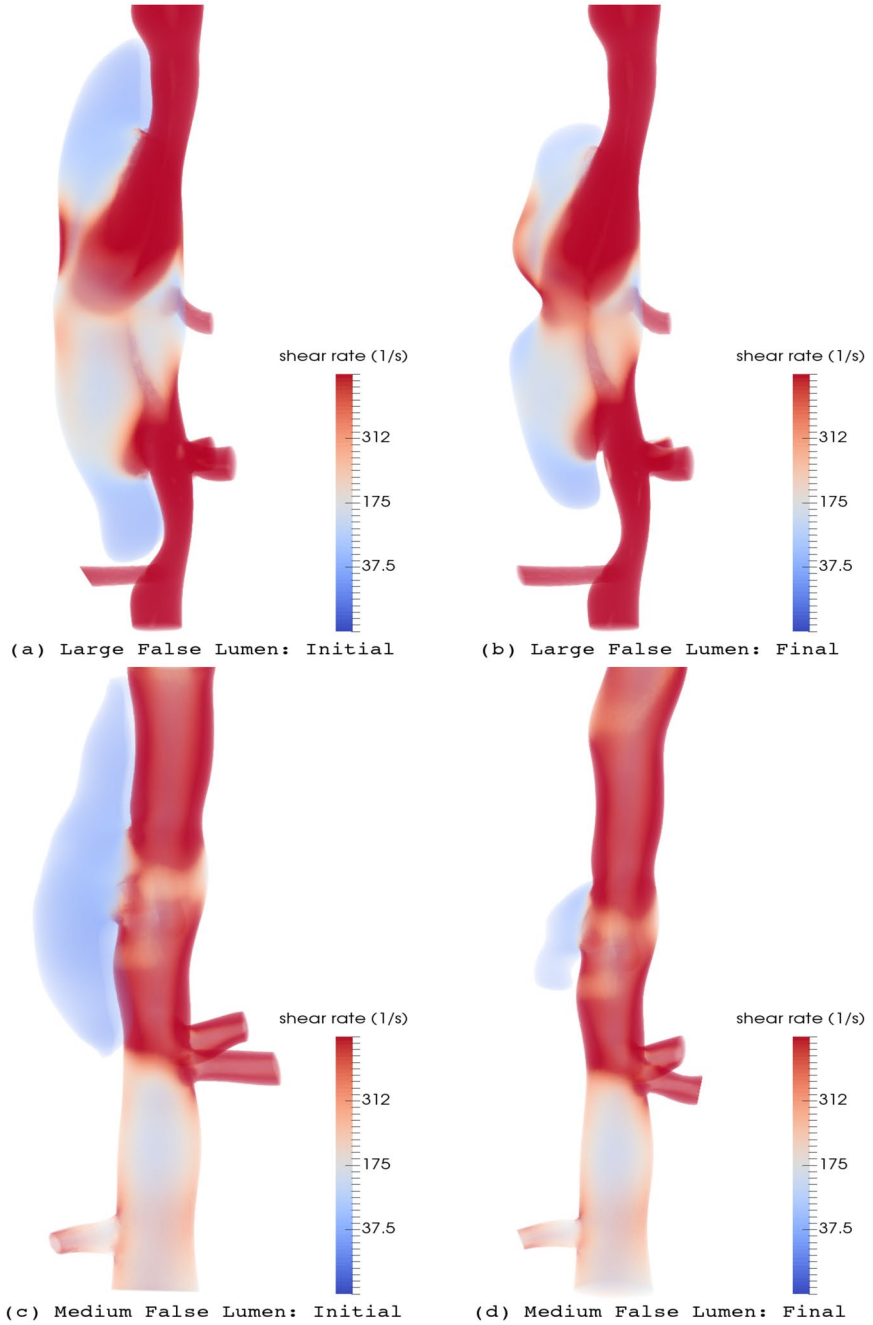


**Figure 8.** Volume rendering of scalar shear rate $\dot{\gamma}$ at peak systole for two lesions at the initial (left) and final (right) stages of thrombus formation upon dissection (blood flow direction is from top to bottom in all cases): (**a**),(**b**) for large false lumen; (**c**),(**d**) for medium false lumen.

geometry and flow conditions and the large size of aortic dissections may require hundreds of thousands of FCM particles to represent platelets, which imposes a restrictively high computational cost for such simulations in large domains. To overcome this difficulty, we made the following assumptions: first, we assumed that upon the initial tear and dissection event, blood, consisting of platelets and other agonists (clotting factors), completely fills the open false lumen; second, we drastically reduced the number of particles by assuming that each particle can become a pseudo-platelet that grows in size upon activation; finally, we disregarded the complex and parameter sensitive enzymatic reactions in the coagulation cascade as we observed that hemodynamics play a major role in the transport of particles and the stabilization of thrombus shape. The increase in the size of particles upon activation is crucial in reducing the number of platelets in the domain and, hence, accelerating the process of thrombus formation. These numerical treatments collectively enable us to address the short-term process as a *final-value* problem instead of simulating the original initial-value problem.

Long-term remodeling of the thrombus based on the constrained mixture theory[20] will require a continuum representation of the thrombus shape and its composition. Therefore, it is desirable to represent the thrombus

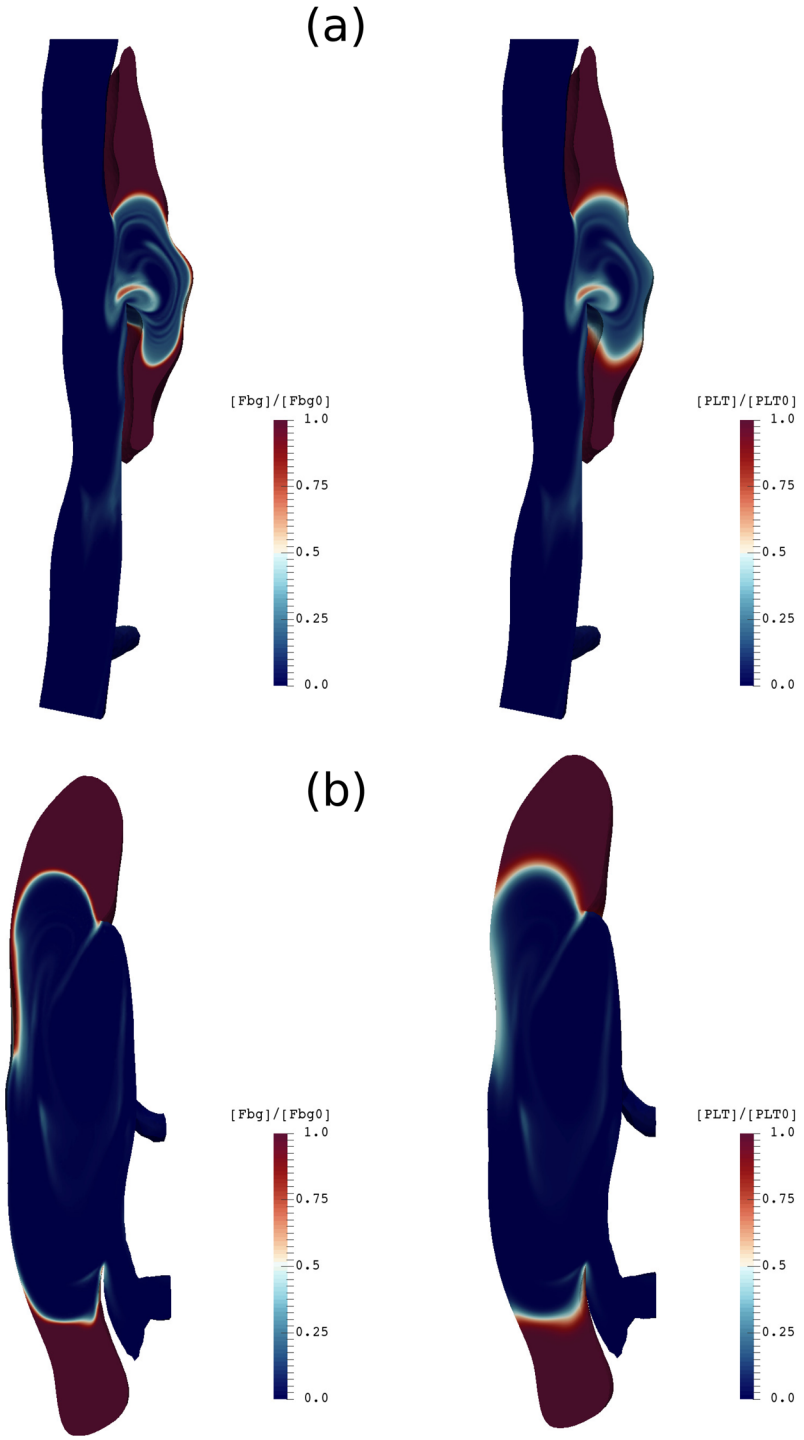


**Figure 9.** Contours of normalized Fbg concentration (left) and platelet concentration (right) plotted on a longitudinal slice along the flow direction (top to bottom) for (**a**) medium and (**b**) large false lumens after 10 cardiac cycles.

as a separate continuous phase field. Volume (or mass) fraction of clot constituents can be estimated using the FCM volume fraction ($\phi_{fcm}$) and local platelet and fibrinogen concentrations. Rheological studies have shown that fibrin clots exhibit viscoelastic behavior[21], which will allow us to model the clot-blood flow interaction using a phase-field approach and a multiphase formulation[21]. Further, the transport of other relevant concentrations of biochemicals to fibrinolysis (*e.g.*, plasminogen) may be modeled in blood (single-phase) and within the thrombus (multiphase) through a multiphasic approach. We will address the issue of long-term remodeling of thrombus and its interaction with blood in a separate study.

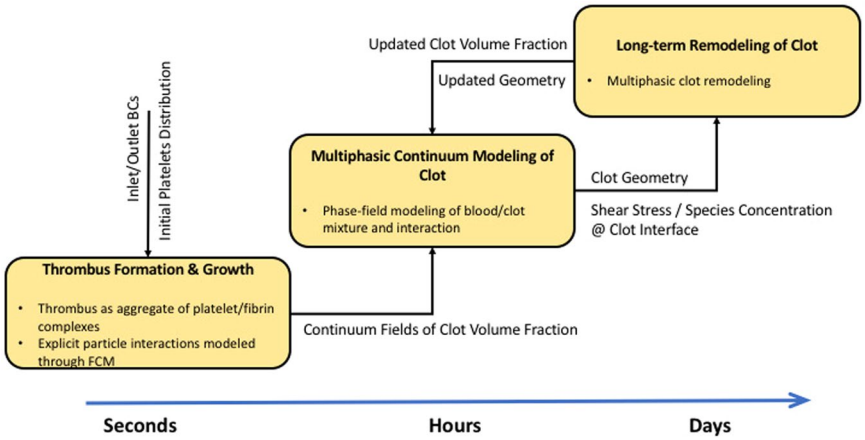


**Figure 10.** The proposed multiscale numerical model of thrombus formation and growth/remodeling of the remnant wall in a dissecting aneurysm. The platelet activation/aggregation model, based on FCM, is the most expensive module in this framework and, thus, is only used to model the formation and propagation of the clot for several seconds after dissection. Once a stable intramural thrombus is formed, we transform the platelet Lagrangian distribution in the aggregate clusters into continuum fields of clot volume fraction, which can be subsequently used in a phase-field numerical approach to model interaction of blood with thrombus, and its further remodeling.

In the present study, we were mainly interested in the acute size and shapes of the false lumen, thrombus, and initial rather than the long-term evolution. We accelerated the process several-fold by (i) distributing particles uniformly inside the initial false lumen assuming that blood enters the false lumen upon onset of dissection and platelets are almost everywhere, (ii) assuming that all dissected mural surfaces expose the blood to damaged collagen and are thus thrombogenic. Hence, platelets in the vicinity of the wall become activated and can adhere to the walls; once activated, they grow up to 20 times larger by turning into pseudo-particles that bear the physiologic density of platelets and concentration of fibrin. Clearly, the presence of activated platelets is essential in the progression of thrombus formation. Shear-induced activation of platelets due to an accumulated stress history can also stimulate platelets in high-shear flow conditions, such as blood flow through atherosclerotic plaques and mechanical heart valves[22,23], or even abdominal aortic aneurysms[24–26]. We did not consider shear history since we felt that biochemical effects dominate with wall damage. Nevertheless, Menichini *et al*. employed a mechanical activation model to incorporate the shear stress history of platelets along their trajectories and found that the highest activation levels occur for platelets crossing the entry tear when transported into the false lumen. The time-averaged wall shear stress close to the entry tear in their human study was about 20 $Pa$, which is significantly higher than values in the present study of murine dissection ($<1\,Pa$). Therefore, in our model, only resting platelets that are within a short distance of the damaged wall will be initially activated while other platelets will become activated via contact.

In the FCM method, inter-particle forces are transferred to the carrier fluid through smooth Gaussian kernels. Using the same kernels, we generated continuous fields of volume fractions for the distribution of particles. Volume fraction $\phi_{fcm}$ served two purposes in our study. First, it works as an indicator function as to where thrombus is more likely to form in the false lumen, which in turn, shows boundaries of the thrombi (*e.g*., Fig. 4). Second, it identifies regions in which more platelets adhere and, hence, thrombus is denser (indicated by higher $\phi_{fcm}$ values) versus regions where shear rates are higher and less deposition occurs (lower $\phi_{fcm}$ values). The agreement achieved between the simulated and observed boundaries of the thrombus, despite uncertainties in numerical parameters and experimental measurements, confirms the general ability of our approach. In addition, the sensitivity tests based on different adhesive parameters, pseudo-platelet sizes, and Reynolds numbers showed that the model is robust, though some improvements will be needed for better accuracy. Detailed analyses of the final shapes of the false lumen show only slight deviations in a few regions, such as slice C in the medium false lumen (Fig. 5) and slices A and C in the large false lumen (Fig. 7). The common feature for all of these regions is the locally high shear rates. Currently, our FCM model is calibrated for flow regimes inside the false lumen and presumably controlled by low-shear conditions. Therefore, particle adhesive forces are not adjusted in the regions of elevated shear rates, which may have led to the mentioned deviations. A shear-dependent calibrated model[12] could improve the numerical predictions further. Presenting quantitative evaluations of differences between simulation and experiment could become somewhat difficult as spatial variation of thrombus shape is significant and depends on local flow conditions.

Because the FCM volume fraction cannot determine the composition of a clot in terms of its dominant constituents, we considered transport of the most important species that contribute to a clot, namely fibrinogen and platelets. Knowing local concentrations of these components along with $\phi_{fcm}$, and using an empirical correlation, we were able to estimate the volume fraction of clot through Eq. (11). For example, in experimental work by[27], the fiber volume fraction was estimated by the empirical relation $\phi_f = c_{Fbg}/[\rho_{Fbg}(0.015\log(c_{Fbg}) + 0.13)]$, where $c_{Fbg}$ (in $mg/mL$), is a key parameter, with $\rho_{Fbg} = 1.4\,g/mL$ the density of a single fibrinogen protein. Further, the volume

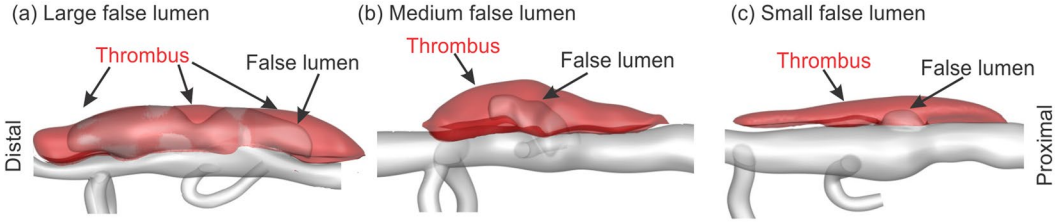


**Figure 11.** Reconstructed geometries from 3D ultrasound and OCT image stacks of three dissections of the suprarenal aorta in the $ApoE^{-/-}$ mouse; cf[16]. for a description of the original data. The shaded red volume represents the thrombus whereas the pink volume is the false lumen with flowing blood; the grey shows the patent vessel. The direction of flow is from right to left, that is, from the proximal to the distal end.

fraction contribution of platelets $\phi_p$ can be directly evaluated based on each platelet's volume (assuming a spherical particle of radius 1.5 $\mu m$) and the local platelet number density.

Solving the transport Eq. (9) is normally cheaper than using particles coupled with the flow solver. Therefore, it is straightforward to perform parallel pilot simulations in the patent false lumen to estimate platelet and fibrinogen/fibrin concentrations that can be used in the evaluation of clot volume fraction. Further, note that the transport Eq. (9) for platelets can be used to estimate platelet residence times in a similar fashion. Evidence suggests that regions with higher residence times are more prone to initiate thrombus and further growth[19,24]. Having accurate spatio-temporal measurements of clot volume fraction $\phi_c$ is essential for long-term growth and remodeling simulations. Multiphasic modeling of blood and clot interaction along with clot remodeling from an initially fibrin-dominated structure to a collagenous mass[28] using a constrained mixture model will be important to simulate as well.

In conclusion, we present for the first time a particle-continuum numerical model to predict acute thrombus size and shape within aortic dissections. The numerical method is based on a two-way coupling of Lagrangian particle transport with blood, where a phenomenological model for inter-particle forces is used to mimic platelet adhesion and aggregation. Our numerical results show strong effects of hemodynamics on thrombus growth, and, thus, final shapes of false lumen. These results were previously reported as experimental findings for three classes of murine suprarenal aortic dissections[16]. The availability of three different lesions was extremely important in the calibration of our model and in performing posterior analyses of numerical results. Numerical predictions of the location and extent of thrombus is satisfactory, and we seek to extend the model to human dissections, which could be beneficial to clinical decisions regarding appropriate treatments.

## Methods

Aortic dissection was induced via a standard subcutaneous infusion of AngII at a rate of 1000 *ng/kg/min* in adult male $ApoE^{-/-}$ mice. Multi-modal imaging data, obtained by combining 3D ultrasound and optical coherence tomography (OCT), were previously used to construct computational domains while pulsed wave Doppler and anatomic 3D ultrasound were used to estimate the average flow velocities at the inlet, outlet, and four branches of the aorta[16]. Herein, we consider three classes of aortic dissection that did not rupture (Fig. 11): one with a large false lumen with little thrombus, one with considerable thrombus but a modest residual false lumen, and one that is largely filled with thrombus. All experimental procedures were approved by the Institutional Animal Care and Use Committee (IACUC) at Purdue University and were carried out in accordance with the approved guidelines[16].

**Particle-Continuum model.** Due to the long-time evolution of intramural thrombus, formation, maturation, and remodeling within the false lumen, a multiscale approach is necessary. More specifically, it is best to decompose the entire process into two main parts: first, the initiation and formation of thrombus within the false lumen, which occurs on the order of minutes to hours following the dissection and, second, the growth and remodeling of the clot, which is mainly related to fibrin degradation and collagen production, which occurs on the order of days to weeks[28]. In this paper, we focus on the former–the acute phase that establishes the initial size and shape of the clot. Toward this end, we focus on the platelet activation, aggregation, and formation of the initial fibrin mesh.

*Modeling platelet transport and aggregation using FCM.* The motion of platelets within a flow field and their adhesion to a damaged intramural dissection surface are solved together by coupling a spectral/hp element method (SEM)[29] with a force coupling method (FCM) similar to the work of Pivkin *et al.*[30]. Specifically, SEM is used to solve the flow field on a fixed Eulerian grid, whereas FCM is implemented to describe the two-way interactions between the blood flow and platelets. Due to the high concentration of fibrinogen in blood, and therefore initially within a dissection, and fairly weak flow conditions inside the initial false lumen, the clot is considered to consist mainly of fibrin[31]. Fibrin monomers polymerize and form networks that capture platelets and other blood cells to form a loosely packed, porous clot. In our model, platelets are assumed to exist in three different states, namely *passive*, *triggered*, or *activated*, as first proposed in[30]. In passive or triggered states, platelets have their physiological radius of $r_p = 1.5\ \mu m$ and are non-adhesive (Fig. 12a). Initially, passive platelets are distributed uniformly inside the false lumen (Fig. 12a), assuming that the initial engorgement of the newly created false lumen would allow the blood particles to mix well. If a passive platelet interacts with an activated platelet or the damaged

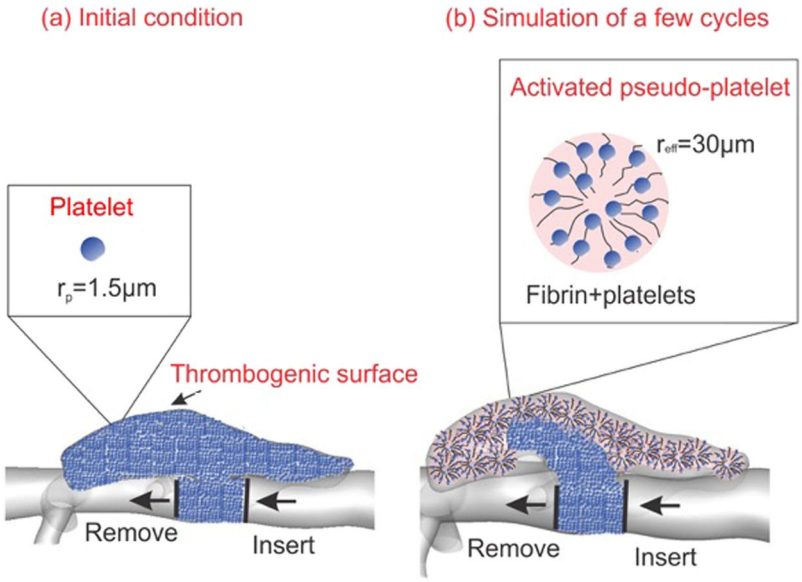


**Figure 12.** (**a**) Initial platelet distribution in the instantaneous false lumen, with the actual thrombus removed numerically. Also shown are locations along the artery where new platelets are inserted into the domain and outgoing platelets are deleted from the simulation. *Inset:* passive platelets as spherical particles of radius $r_p = 1.5\,\mu m$. (**b**) Platelets change their size once they come into contact with the dissected wall and become activated, catalyzing the conversion of blood borne fibrinogen into semi-solid fibrin–*Inset:* activated platelets with increased effective radius $r_{eff} = 20 - 40 r_p$.

wall bounding the false lumen, however, it becomes triggered and switches to an activated state after delay time $\tau_{act} = 0.1 - 0.3\,s$. Upon activation, pseudo-platelets (*i.e.*, platelets and associated fibrin) grow in size to an effective radius $r_{eff}$ (Fig. 12b). This approach allows us to use fewer platelets than the physiologic concentration and to grow the size and shape of the clot once the platelets come in contact with the injured wall or each other.

The FCM has been described in detail previously[12]. Briefly, the translational velocity of each platelet (passive or activated) is estimated by the local average of the fluid velocity weighted by a Gaussian kernel function. The governing equations for the incompressible flow are the mass balance (continuity) and linear momentum balance (Navier-Stokes) equations

$$\nabla \cdot \mathbf{u} = 0, \tag{1}$$

$$\rho\left(\frac{\partial \mathbf{u}}{\partial t} + \mathbf{u} \cdot \nabla \mathbf{u}\right) = -\nabla p + \mu \nabla^2 \mathbf{u} + \mathbf{f}(\mathbf{x}, t), \tag{2}$$

where $\mathbf{u}$, $p$, and $\mu$ are the flow velocity, pressure, and blood viscosity, respectively, with body force $\mathbf{f}$ used to capture the effects of the particles (platelets) on the flow. Specifically,

$$\mathbf{f}(\mathbf{x}, t) = \sum_{n=1}^{N} \mathbf{F}^n \Delta(\mathbf{x} - \mathbf{Y}^n(t)), \tag{3}$$

$$\Delta(\mathbf{X}) = (2\pi\sigma^2)^{-3/2} \exp(-\mathbf{X} \cdot \mathbf{X}/2\sigma^2). \tag{4}$$

Here, $\mathbf{F}^n$ is the force due to particle $n$ in the local region of interest. Moreover, the contribution of each platelet, whose center of mass is located at $\mathbf{Y}^n$, to the flow at position $\mathbf{x}$ is smoothed by a Gaussian distribution kernel $\Delta(\mathbf{X} \equiv (\mathbf{x} - \mathbf{Y}^n))$ with $\sigma$ the standard deviation of the kernel, which is related to particle radius $a = (r_p$ or $r_{eff})$ through $\sigma = a/\sqrt{\pi}$. The governing equations are written in weak form and the domain is discretized using spectral elements that allow high order Jacobi polynomials. Time integration is performed using a semi-implicit splitting scheme[29]. The velocity of each platelet $\mathrm{V}^n$ is calculated by interpolating the local flow velocity at the location of a platelet using the same Gaussian kernel of Eq. (4) although different standard deviations may be used for force and velocity interpolations. Specifically,

$$\mathbf{V}^n = \frac{d\mathbf{Y}^n}{dt} = \int \mathbf{u} \Delta(\mathbf{x} - \mathbf{Y}^n(t)) d\mathbf{x}, \tag{5}$$

where position vectors for all the platelets are updated at each time step using a second-order Euler forward scheme.

Further, the net force $\mathbf{F}^n$ acting on each platelet is written

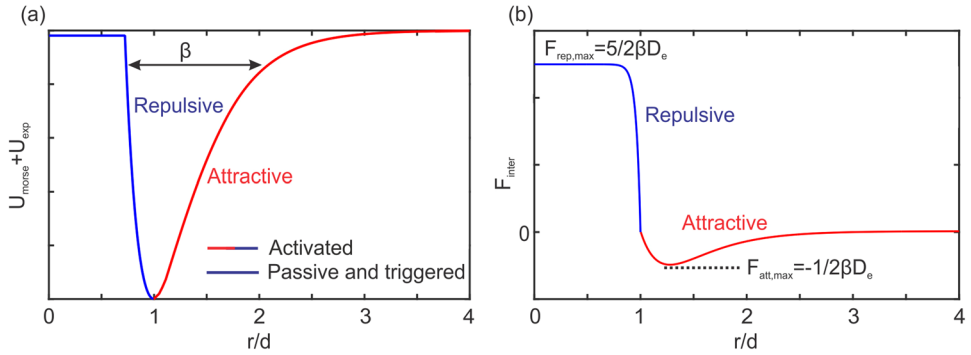


**Figure 13.** Schematic of the Morse + exponential potential (left) and the resulting adhesive force (right) used to mimic inter-platelet attractive/repulsive forces. Passive and triggered platelets only generate repulsive forces to prevent overlap, whereas activated platelets attract each other as well.

$$\mathbf{F}^n = -\frac{4}{3}\pi a^3(\rho_{plat} - \rho_{fluid})\frac{d\mathbf{V}^n}{dt} + \mathbf{F}_{inter}, \tag{6}$$

where the first term is the inertial force resulting from the difference in mass density between the platelets and blood flow and the second term accounts for interaction forces between platelets and the wall, which represent effects of different ligand-receptor interactions. Specifically, $\mathbf{F}_{inter} = -\partial U/\partial r$, where $r$ is the distance between platelet centroids and the potential $U = U_{Morse} + U_{exp}$.

Specifically, we use a phenomenological model based on Morse potential $U_{Morse}$, having units of (Nm), to model attractive interactions between platelets, written as

$$U_{Morse} = D_e[1 - e^{-\beta d(r/d-1)}]^2 \quad r > d, \tag{7}$$

where $D_e$ is the energy depth contributing to the strength of the interaction force, $\beta$ controls the width of the energy well, and $d = 2r_p$ (or $2r_{eff}$ if activated) is the equilibrium distance between two platelets. To avoid instability due to strong Morse repulsive forces, we use an exponential repulsion potential in the form of

$$U_{\exp} = \frac{A}{1 - e^{Br_c}}\left[e^{Br_c}r - \frac{e^{Br}}{B}\right] \quad r < d, \tag{8}$$

where the parameter $A$ defines the maximum repulsive strength as $r \to 0$, $B$ is an adjustable parameter that defines the shape of the repulsive force (see Fig. 13b), and $r_c$ is the cutoff radius. By setting $B$ to a large positive number (here $B = 25$ in nondimensional units) and letting $r_c = d$, we obtain a hard-sphere repulsive potential. We set the parameter $A$ such that the ratio of maximum repulsive to attractive forces is 5 (Fig. 13b). Unlike the standard Morse repulsion, the exponential repulsion does not become singular as $r \to 0$, which eliminates potential instabilities in particle systems.

The value of $\beta d$ defines the range of interactions between platelets; it is selected to be 2.5 to prevent overlap of passive platelets though partial overlap is allowed for activated platelets ($F_{rep,max}/|F_{att,max}| = 5$). The Morse attractive force is negligible for $r/d > 3$, which is considered as the cutoff radius for the attractive forces to avoid long-range interactions. The undetermined parameter $D_e$, which controls the magnitude of platelet interaction forces, and $r_{eff}$, which controls the number of particles in the simulation, are estimated by comparing the simulated thrombus size and shape against experimental observations[16] under the same hemodynamic conditions. To calibrate the platelet aggregation model, we consider an interaction distance of $2d$ between platelets within which resting platelets may become activated.

*Platelets and fibrinogen transport.* We solve the transport of platelets and fibrinogen (denoted Fbg) using an advection/diffusion equation:

$$\frac{\partial c}{\partial t} + \mathbf{u} \cdot \nabla c = D_{eff}\nabla^2 c, \tag{9}$$

where $c$ is the concentration field and $D_{eff}$ is the shear-induced effective diffusion coefficient. The physiologic concentration of Fbg in blood is $c^o_{Fbg} = 7\ \mu M$[32]. Transport of platelets is modeled by treating platelet concentration as a continuum field, with $\approx 4 \times 10^5$ platelets per $mm^3$ of blood. The effective diffusion coefficient for platelets and macromolecules (*e.g.*, Fbg) due to presence of red blood cells is taken as a function of the local shear rate based on an equation proposed by Wootton *et al.*[33], $D_{eff} = D_{br} + \alpha\dot{\gamma}$, where the Brownian diffusion $D_{br}$ is $1.58 \times 10^{-13}$ and $3.1 \times 10^{-11}\ m^2/s$ for Fbg and platelets, and the coefficient $\alpha$ is $6.0 \times 10^{-14}$ and $7.0 \times 10^{-13}\ m^2$ for Fbg and platelets, respectively[33,34]. Herein, we introduced two assumptions to reduce the complexity of the transport problem: first, we let the value of shear rate inside the false lumen be $\dot{\gamma} \approx 100\ s^{-1}$ (see comments in

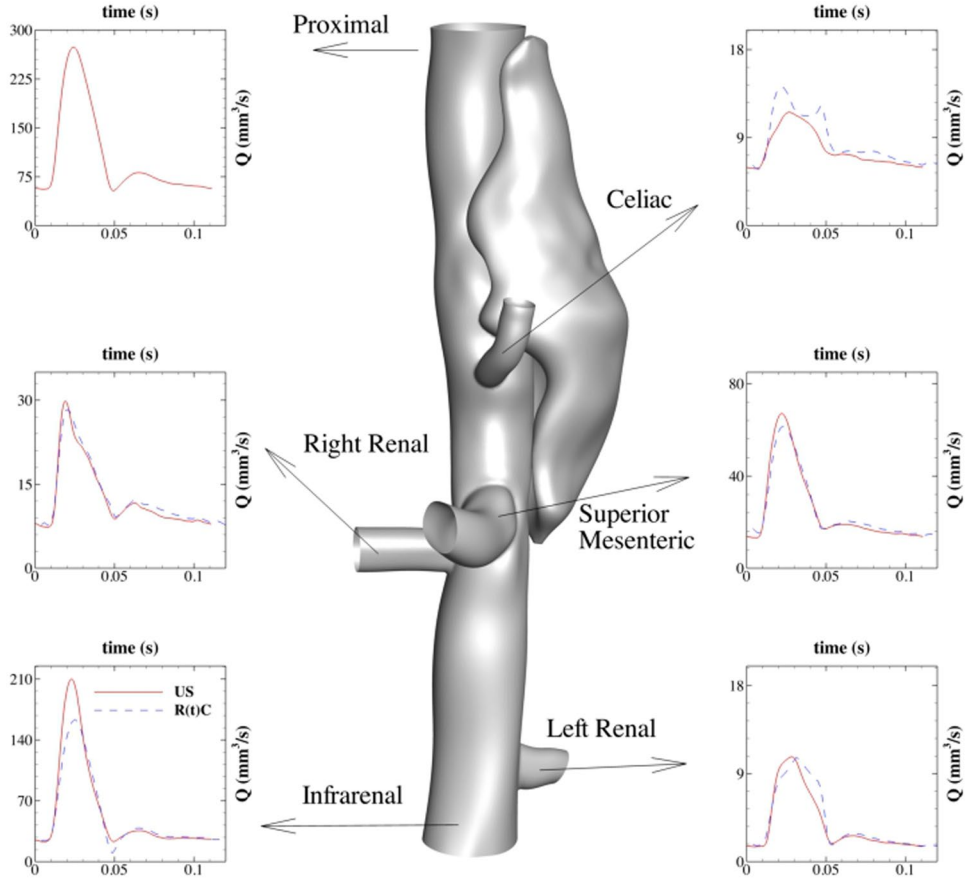


**Figure 14.** Inlet/outlet boundary conditions for the lesion with the medium false lumen: a Dirichlet flow waveform measured by ultrasound[16] is imposed at the proximal inlet, while Windkessel RC type boundary conditions are prescribed at every main outlet branch. A time-dependent resistance R(t) is estimated based on the experimental flow waveforms to improve the accuracy (shown in the inset plot for each outlet).

Discussion) to be consistent with the flow simulations and to allow a uniform value of the diffusion coefficient; second, to avoid spurious solutions at high Peclet numbers (where $Pe = D_{eff}U_{avg}/\nu \approx 10^6$, with the mean velocity $U_{avg}$ at inlet, and the blood kinematic viscosity $\nu$), which requires special treatment in the numerical scheme and typically leads to long and expensive simulations to reach the desired static solutions, we increase the diffusion coefficients by two orders of magnitude. Hence, the final values of $D_{eff}$ are $6.16 \times 10^{-10}$ and $1.01 \times 10^{-8}$ $m^2/s$ for fibrinogen and platelets, respectively. All concentrations are normalized by physiologic values, with the initial distribution of Fbg and platelets assumed homogeneous everywhere.

*Clot volume fraction estimation.* To analyze the evolution in thrombus size and shape and to anticipate future simulations of multiphasic, long-term remodeling, we used a continuum representation of the adhered pseudo-platelets in the clot. This can be achieved easily in the context of the FCM by estimating the local volume fraction of FCM particles as:

$$\phi_{fcm}(\mathbf{x}, t) = \sum_{n=1}^{N} \mathcal{V}_p^{\,n} \Delta(\mathbf{x} - \mathbf{Y}^n(t)), \tag{10}$$

where $\mathcal{V}_p^{\,n} = 4\pi a_n^3/3$ is the volume of each FCM particle. A larger standard deviation ($\sigma \approx 4d$) in the Gaussian kernel in Eq. (4) yields a smooth representation of $\phi_{fcm}$.

Knowing the local concentration of fibrinogen and platelets, and using the estimated $\phi_{fcm}$ field, we can evaluate clot volume fraction $\phi_c$ as:

$$\phi_c = \left[\phi_f(c_{Fbg}) + \phi_p(c_{plat})\right] \phi_{fcm}, \tag{11}$$

where an empirical correlation relates fibrin volume fraction $\phi_f$ to the concentration of Fbg, and $\phi_p$ denotes the platelet volume fraction[27]. Further details regarding the estimation of $\phi_f$ and $\phi_p$ can be found in the Discussion.

*Flow and concentration boundary conditions.* Mouse-specific inlet flow rate waveforms were prescribed individually at the level of the proximal suprarenal aorta as a Dirichlet boundary condition (using a Womersley velocity profile[35]) based on pulsed wave Doppler measurements taken at the same location[16]. Two-parameter (also known as RC) Windkessel models were used to match PW Doppler measurements in the major outlet vessels (see Fig. 14). A detailed study on robustness and stability of different outflow boundary conditions showed that two-parameter (RC) models are more stable than three-parameter (RCR) models[36]. The choice of two-parameter model implies less uncertainty as parameter estimation is not needed for the additional resistance.

Using the average flow rates at each outlet and the flow analysis in a network of vessels given in[36], we are able to calculate the steady RC values for each outlet. Our numerical observations, however, showed that the steady RC values do not perform well in the vasculature with the dissection, where the flow dynamics is significantly affected by the presence of the false lumen. Taking advantage of flow waveforms at the outlets, we computed time-dependent R(t)C values to reproduce the flow waveforms more effectively (shown in Fig. 14). A zero-flux Neumann boundary condition for velocity was considered at each outlet.

At the proximal inlet, the insertion of platelets is governed by the inlet flow waveform and by a master profile for platelets distribution taking into account the margination of platelets in the proximal suprarenal aorta[18]. Further, to solve the transport of Fbg and platelets within the false lumen using Eq. (9), we assumed zero concentration at the proximal inlet and a zero-flux Neumann boundary condition at each outlet.

**Data Availability.** All data generated or analyzed during this study are included in this published article (and its Supplementary Information files).

## References


1. Jain, D., Dietz, H. C., Oswald, G. L., Maleszewski, J. J. & Halushka, M. K. Causes and histopathology of ascending aortic disease in children and young adults. *Cardiovascular Pathology* **20**, 15–25 (2011).
2. Tsai, T. T. *et al*. Partial thrombosis of the false lumen in patients with acute type b aortic dissection. *New England Journal of Medicine* **357**, 349–359 (2007).
3. Song, S.-W. *et al*. Effects of early anticoagulation on the degree of thrombosis after repair of acute debakey type i aortic dissection. *The Annals of thoracic surgery* **92**, 1367–1375 (2011).
4. Tsai, T. T. *et al*. Tear size and location impacts false lumen pressure in an *ex vivo* model of chronic type b aortic dissection. *Journal of vascular surgery* **47**, 844–851 (2008).
5. Daugherty, A., Manning, M. W. & Cassis, L. A. Angiotensin ii promotes atherosclerotic lesions and aneurysms in apolipoprotein e–deficient mice. *The Journal of clinical investigation* **105**, 1605–1612 (2000).
6. Tse, K. M., Chiu, P., Lee, H. P. & Ho, P. Investigation of hemodynamics in the development of dissecting aneurysm within patient-specific dissecting aneurismal aortas using computational fluid dynamics (cfd) simulations. *Journal of biomechanics* **44**, 827–836 (2011).
7. Clough, R. E. *et al*. A new method for quantification of false lumen thrombosis in aortic dissection using magnetic resonance imaging and a blood pool contrast agent. *Journal of vascular surgery* **54**, 1251–1258 (2011).
8. Dillon-Murphy, D., Noorani, A., Nordsletten, D. & Figueroa, C. A. Multi-modality image-based computational analysis of haemodynamics in aortic dissection. *Biomechanics and modeling in mechanobiology* **15**, 857–876 (2016).
9. Karmonik, C. *et al*. Computational fluid dynamics investigation of chronic aortic dissection hemodynamics versus normal aorta. *Vascular and endovascular surgery* **47**, 625–631 (2013).
10. Neeves, K., Illing, D. & Diamond, S. Thrombin flux and wall shear rate regulate fibrin fiber deposition state during polymerization under flow. *Biophysical journal* **98**, 1344–1352 (2010).
11. Wootton, D. M. & Ku, D. N. Fluid mechanics of vascular systems, diseases, and thrombosis. *Annual review of biomedical engineering* **1**, 299–329 (1999).
12. Yazdani, A., Li, H., Humphrey, J. D. & Karniadakis, G. E. A general shear-dependent model for thrombus formation. *PLoS Computational Biology* **13**, e1005291 (2017).
13. Diamond, S. L. Systems analysis of thrombus formation. *Circulation research* **118**, 1348–1362 (2016).
14. Zhang, P., Zhang, L., Slepian, M. J., Deng, Y. & Bluestein, D. A multiscale biomechanical model of platelets: Correlating with *in-vitro* results. *Journal of biomechanics* **50**, 26–33 (2017).
15. Zhang, P. *et al*. Multiscale particle-based modeling of flowing platelets in blood plasma using dissipative particle dynamics and coarse grained molecular dynamics. *Cellular and Molecular Bioengineering* **7**, 552–574 (2014).
16. Phillips, E., Di Achille, P., Bersi, M. R., Humphrey, J. D. & Goergen, C. Multi-modality imaging enables detailed hemodynamic simulations in dissecting aneurysms in mice. *IEEE Transactions on Medical Imaging* **36**, 1297–1305 (2017).
17. Boyd, J., Buick, J. M. & Green, S. Analysis of the casson and carreau-yasuda non-newtonian blood models in steady and oscillatory flows using the lattice boltzmann method. *Physics of Fluids* **19**, 093103 (2007).
18. Aarts, P. A. *et al*. Blood platelets are concentrated near the wall and red blood cells, in the center in flowing blood. *Arteriosclerosis, Thrombosis, and Vascular Biology* **8**, 819–824 (1988).
19. Menichini, C., Cheng, Z., Gibbs, R. G. & Xu, X. Y. Predicting false lumen thrombosis in patient-specific models of aortic dissection. *Journal of The Royal Society Interface* **13**, 20160759 (2016).
20. Humphrey, J. & Rajagopal, K. A constrained mixture model for growth and remodeling of soft tissues. *Mathematical models and methods in applied sciences* **12**, 407–430 (2002).
21. Kim, O. V., Xu, Z., Rosen, E. D. & Alber, M. S. Fibrin networks regulate protein transport during thrombus development. *PLOS Comput Biol* **9**, e1003095 (2013).
22. Bluestein, D., Niu, L., Schoephoerster, R. T. & Dewanjee, M. K. Fluid mechanics of arterial stenosis: relationship to the development of mural thrombus. *Annals of biomedical engineering* **25**, 344–356 (1997).
23. Nobili, M., Sheriff, J., Morbiducci, U., Redaelli, A. & Bluestein, D. Platelet activation due to hemodynamic shear stresses: damage accumulation model and comparison to *in vitro* measurements. *ASAIO journal (American Society for Artificial Internal Organs: 1992)* **54**, 64 (2008).
24. Di Achille, P., Tellides, G., Figueroa, C. & Humphrey, J. A haemodynamic predictor of intraluminal thrombus formation in abdominal aortic aneurysms. In *Proc. R. Soc. A*, vol. 470, 20140163 (The Royal Society 2014).
25. Wilson, J. S., Virag, L., Di Achille, P., Karšaj, I. & Humphrey, J. D. Biochemomechanics of intraluminal thrombus in abdominal aortic aneurysms. *Journal of Biomechanical Engineering* **135**, 021011 (2013).
26. Shadden, S. C. & Hendabadi, S. Potential fluid mechanic pathways of platelet activation. *Biomechanics and modeling in mechanobiology* 1–8 (2013).

27. Wufsus, A., Macera, N. & Neeves, K. The hydraulic permeability of blood clots as a function of fibrin and platelet density. *Biophysical journal* **104**, 1812–1823 (2013).
28. Schriefl, A. *et al*. Remodeling of intramural thrombus and collagen in an ang-ii infusion apoe$^{-/-}$ model of dissecting aortic aneurysms. *Thrombosis research* **130**, e139–e146 (2012).
29. Karniadakis, G. & Sherwin, S. *Spectral/hp element methods for computational fluid dynamics*, third edn (Oxford University Press, 2013).
30. Pivkin, I. V., Richardson, P. D. & Karniadakis, G. Blood flow velocity effects and role of activation delay time on growth and form of platelet thrombi. *Proceedings of the National Academy of Sciences* **103**, 17164–17169 (2006).
31. Scott, D. J. A. *et al*. Clot architecture is altered in abdominal aortic aneurysms and correlates with aneurysm size. *Arteriosclerosis, thrombosis, and vascular biology* **31**, 3004–3010 (2011).
32. Anand, M., Rajagopal, K. & Rajagopal, K. A model for the formation, growth, and lysis of clots in quiescent plasma. a comparison between the effects of antithrombin iii deficiency and protein c deficiency. *Journal of Theoretical Biology* **253**, 725–738 (2008).
33. Wootton, D. M., Markou, C. P., Hanson, S. R. & Ku, D. N. A mechanistic model of acute platelet accumulation in thrombogenic stenoses. *Annals of biomedical engineering* **29**, 321–329 (2001).
34. Goodman, P. D., Barlow, E. T., Crapo, P. M., Mohammad, S. F. & Solen, K. A. Computational model of device-induced thrombosis and thromboembolism. *Annals of biomedical engineering* **33**, 780–797 (2005).
35. Womersley, J. R. An elastic tube theory of pulse transmission and oscillatory flow in mammalian arteries. Tech. Rep., DTIC Document (1957).
36. Grinberg, L. & Karniadakis, G. E. Outflow boundary conditions for arterial networks with multiple outlets. *Annals of biomedical engineering* **36**, 1496–1514 (2008).

## Acknowledgements

This work was supported by NIH grant U01HL116323. Computational resources were provided by the Center for Computation and Visualization (CCV) at Brown University, TACC/STAMPEDE and SDSC/COMET through the XSEDE grant (TG-DMS140007), and ANL and ORNL supercomputers through a DOE/INCITE award. The original computational domains and inlet/outlet conditions came from[16], with particular thanks to Professor Craig Goergen at Purdue University.

## Author Contributions

H.L. carried out the simulations and performed analyses; A.Y. performed analyses and participated in the design of the study, drafted the manuscript and the subsequent revisions; P.D.A. performed image analysis and segmentation, and collaborated on the parameter estimation. M.R.B. carried out the OCT experiments and image segmentation; J.I. collaborated on the visualizations and created animations; J.D.H. helped design the study and helped draft and finalize the manuscript; G.E.K. helped design and coordinate the study and helped draft the manuscript. All authors gave final approval for publication.

## Additional Information

**Supplementary information** accompanies this paper at https://doi.org/10.1038/s41598-018-20603-x.

**Competing Interests:** The authors declare that they have no competing interests.

**Publisher's note:** Springer Nature remains neutral with regard to jurisdictional claims in published maps and institutional affiliations.